

## Electrostatic Intraperitoneal Aerosol Delivery of Nanoparticles: Proof of Concept and Preclinical Validation

Van de Sande, Leen; Rahimi-Gorji, Mohammad; Giordano, Silvia; Davoli, Enrico; Matteo, Cristina; Detlefsen, Sönke; D'Herde, Katharina; Braet, Helena; Shariati, Molood ; Remaut, Katrien; Xie, Feifan; Debbaut, Charlotte; Ghorbaniasl, Ghader; Cosyns, Sarah; Willaert, Wouter; Ceelen, Wim

*Published in:*  
Advanced Healthcare Materials

*DOI:*  
[10.1002/adhm.202000655](https://doi.org/10.1002/adhm.202000655)

*Publication date:*  
2020

*License:*  
Unspecified

*Document Version:*  
Accepted author manuscript

[Link to publication](#)

### *Citation for published version (APA):*

Van de Sande, L., Rahimi-Gorji, M., Giordano, S., Davoli, E., Matteo, C., Detlefsen, S., D'Herde, K., Braet, H., Shariati, M., Remaut, K., Xie, F., Debbaut, C., Ghorbaniasl, G., Cosyns, S., Willaert, W., & Ceelen, W. (2020). Electrostatic Intraperitoneal Aerosol Delivery of Nanoparticles: Proof of Concept and Preclinical Validation. *Advanced Healthcare Materials*, 9(16). <https://doi.org/10.1002/adhm.202000655>

### Copyright

No part of this publication may be reproduced or transmitted in any form, without the prior written permission of the author(s) or other rights holders to whom publication rights have been transferred, unless permitted by a license attached to the publication (a Creative Commons license or other), or unless exceptions to copyright law apply.

### Take down policy

If you believe that this document infringes your copyright or other rights, please contact [openaccess@vub.be](mailto:openaccess@vub.be), with details of the nature of the infringement. We will investigate the claim and if justified, we will take the appropriate steps.

## Electrostatic Intraperitoneal Aerosol Delivery of Nanoparticles: Proof of Concept and Preclinical validation

*Leen Van de Sande#, Mohammad Rahimi-Gorji#, Silvia Giordano, Enrico Davoli, Cristina Matteo, Sönke Detlefsen, Katharina D'Herde, Helena Braet, Molood Shariati, Katrien Remaut, Feifan Xie, Charlotte Debbaut, Ghader Ghorbaniasl, Sarah Cosyns, Wouter Willaert, Wim Ceelen\**

---

L. Van de Sande, M. Rahimi-Gorji, Prof. Dr. K. D'Herde, Dr. S. Cosyns, Prof. Dr. W. Willaert, Prof. Dr. W. Ceelen

Department of Human Structure and Repair, Ghent University

Corneel Heymanslaan 10

9000 Ghent, Belgium

L. Van de Sande, M. Rahimi-Gorji, H. Braet, Dr. M. Shariati, Prof. Dr. K. Remaut, Prof. Dr. C. Debbaut, Dr. S. Cosyns, Prof. Dr. W. Willaert, Prof. Dr. W. Ceelen

Cancer Research Institute Ghent (CRIG), Ghent University

Corneel Heymanslaan 10

9000 Ghent, Belgium

M. Rahimi-Gorji, Prof. Dr. Debbaut

IBiTech - bioMMeda, Ghent University

Corneel Heymanslaan 10

9000 Ghent, Belgium

Prof. Dr. S. Giordano, Prof. Dr. E. Davoli

Mass Spectrometry Laboratory, Istituto di Ricerche Farmacologiche Mario Negri IRCCS

Via Mario Negri 2

20156 Milan, Italy

C. Matteo

Cancer Pharmacology Laboratory, Istituto di Ricerche Farmacologiche Mario Negri IRCCS

This is the author manuscript accepted for publication and has undergone full peer review but has not been through the copyediting, typesetting, pagination and proofreading process, which may lead to differences between this version and the [Version of Record](#). Please cite this article as [doi: 10.1002/adhm.202000655](https://doi.org/10.1002/adhm.202000655).

Via Mario Negri 2

20156 Milan, Italy

Prof. Dr. S. Detlefsen

Department of Pathology, Odense University Hospital

J.B. Winsløws Vej 4

5000 Odense, Denmark

Prof. Dr. S. Detlefsen

Department of Clinical Research, University of Southern Denmark

Winsløwsparken 19

5000 Odense, Denmark

H. Braet, Dr. M. Shariati, Prof. Dr. K. Remaut

Laboratory of General Biochemistry and Physical Pharmacy, Faculty of Pharmaceutical Sciences,  
Ghent University

Ottergemsesteenweg 460

9000 Ghent, Belgium

Dr. F. Xie

Laboratory of Medical Biochemistry and Clinical Analysis, Faculty of Pharmaceutical Sciences, Ghent  
University

Ottergemsesteenweg 460

9000 Ghent, Belgium

Prof. Dr. G. Ghorbaniasl

Department of Mechanical Engineering, Vrije Universiteit Brussel (VUB)

Pleinlaan 2

1050 Brussels, Belgium

Prof. Dr. W. Ceelen

Department of Human Structure and Repair, Ghent University

Corneel Heymanslaan 10

9000 Ghent, Belgium

#Equal contribution

Keywords: electrostatic precipitation, electromotive drug administration, computational fluid dynamics, intraperitoneal drug delivery, PIPAC

There is an increasing interest in intraperitoneal delivery of chemotherapy as an aerosol in patients with peritoneal metastasis. The currently used technology is hampered by inhomogeneous drug delivery throughout the peritoneal cavity because of gravity, drag, and inertial impaction. Addition of an electrical force to aerosol particles, exerted by an electrostatic field, could improve spatial aerosol homogeneity and enhance tissue penetration. A computational fluid dynamics model shows that electrostatic precipitation (EP) results in a significantly improved aerosol distribution. Fluorescent nanoparticles remain stable after nebulization in vitro, while EP significantly improved spatial homogeneity of nanoparticle distribution. Next, pressurized intraperitoneal chemotherapy (PIPAC) with and without EP using nanoparticle albumin bound paclitaxel (Nab-PTX) in a novel rat model is examined. EP does not worsen the effects of CO<sub>2</sub> insufflation and intraperitoneal Nab-PTX on mesothelial structural integrity or the severity of peritoneal inflammation. Importantly, EP significantly enhances tissue penetration of Nab-PTX in the anatomical regions not facing the nozzle of the nebulizer. Also, the addition of EP leads to more homogeneous peritoneal tissue concentrations of Nab-PTX, in parallel with higher plasma concentrations. In conclusion, EP enhances spatial homogeneity and tissue uptake after intraperitoneal nebulization of anticancer nanoparticles.

## 1. Introduction

Treatment of peritoneal metastasis (PM) remains a challenge in contemporary oncology practice. Many patients present with widespread, unresectable disease, resulting in a dismal prognosis and debilitating symptoms such as obstruction of the gastro-intestinal or urinary tract. Recently, a novel clinical treatment modality was introduced for this patient group, consisting of intraperitoneal (IP) nebulization of chemotherapy during laparoscopy (Pressurized IntraPeritoneal Aerosol Chemotherapy, PIPAC).<sup>[1]</sup> Advantages of PIPAC include the benefits of a minimally invasive approach, the possibility to administer repeated treatments and to take biopsies, and the potential for enhanced tissue drug penetration due to the elevated intra-abdominal pressure during laparoscopy (approximately 12 mmHg).<sup>[2]</sup> Particularly appealing is the possibility for IP nebulization of nanosized drugs such as albumin bound chemotherapy or nucleic acids.<sup>[3–5]</sup>

Despite promising early clinical results, the efficacy of PIPAC is currently limited by inhomogeneous aerosol distribution due to gravity, inertial impaction and drag effects.<sup>[6]</sup> A promising method to overcome spatial heterogeneity during IP aerosol delivery is to apply an external electrostatic field, which exerts an additional force that counteracts the effects of gravity and drag. A commercially available electrostatic generator, marketed to deposit surgical coagulation smoke during laparoscopic surgery, has already been combined with PIPAC in clinical practice.<sup>[7,8]</sup>

Another advantage of combining aerosol delivery with an electrostatic field is the potential to enhance tissue drug penetration by exploiting electromotive forces. Several applications of electromotive drug administration are in clinical use. Intravesical drug administration combined with a local electrical field is used for early stage bladder cancer, but efficacy is uncertain and the underlying mechanisms poorly understood.<sup>[9,10]</sup> Transdermal drug delivery has been combined with sonophoresis, iontophoresis, and electroporation.<sup>[11]</sup> During pulmonary aerosol inhalation, even neutral aerosol particles acquire an electrostatic charge by triboelectric effects, and the magnitude

of this charge was shown to correlate with the deposition fraction of small (0.1-1  $\mu\text{m}$ ) aerosol particles.<sup>[12,13]</sup>

Clearly, there is a significant potential to enhance the efficacy of PIPAC by the addition of an electromotive force. However, the underlying mechanisms remain unexplored, and in vivo studies investigating aerosol distribution and drug delivery are lacking. Here, we report the first systematic investigation of electrostatically enhanced IP aerosol delivery, starting from a computational model which is validated by in vitro and animal experiments.

## 2. Results

### 2.1. Model prediction and in vitro validation of aerosol distribution with and without electromotive force

Based on the dimensions of the in vitro box (185 x 135 x 152 mm<sup>3</sup>, **Figure 1A**), a computational fluid dynamics (CFD) model was developed to predict aerosol distribution with and without EP. **Figure 1B** visualizes the electrical field in this CFD model. Simulations of the aerosol particle distribution after nebulization showed, as expected, prominent effects of gravity and inertial impaction, resulting in near absence of aerosol deposition at position D (top of the box, **Figure 1C**). However, when applying an electrostatic field, a much more homogeneous aerosol distribution was obtained (**Figure 1D**).

Black ink was aerosolized in the in vitro box model to validate the predicted results of the CFD model. In vitro, no significant differences in the proportion of ink stained omental tissue were observed at positions A and B, except for a significant difference between PIPAC and ePIPAC<sub>1min</sub> at location A (**Figure 2A**). However, EP markedly enhanced tissue ink staining of specimens located at the side wall of the box (location C) and at the top of the box (location D). These findings were in

accordance with the mean cryosection scores (**Figure 2B** and **Figure 2C**). The extent of histology scored ink staining did not differ between PIPAC, ePIPAC<sub>1min</sub>, and ePIPAC<sub>30min</sub> at locations A and B. On the contrary, histology scored omental tissue staining was significantly more intense after PIPAC compared to ePIPAC<sub>30min</sub> at location C (side wall) and, although not statistically significant, at the top of the box (location D).

**Figure 3** compares the in silico and in vitro results of spatial distribution of black ink. The computational model predicted effect of the electrostatic charge on aerosol distribution agrees with the experimental results. The slightly lower estimates by the CFD model are explained by the fact that the Measurement Accumulator in COMSOL Multiphysics only considers completely black coverage of tissue, while dark grey was considered as well in vitro. Specifically, both the model and the experimental results show a significantly better aerosol deposition at the top of the box (plate D) when an electrical force is applied.

## 2.2. Effects of high-pressure nebulization on size and charge of nanoparticles

To study the influence of high-pressure nebulization on the physicochemical properties (e.g. size, charge) of NPs, 100 nm and 200 nm NPs were examined before and after nebulization. **Figure 4A** shows that the size of the 100 nm and 200 nm NPs measured by single particle tracking is not significantly increased after nebulization ( $p = 0.228$  and  $0.414$ , respectively). Similar results, however, with a trend to significance, were found when size distribution of the 100 nm and 200 nm NPs was analysed based on dynamic light scattering ( $p = 0.058$  and  $0.105$ , respectively; **Figure 4B**). In general, the size of the NPs is not noticeably changed after nebulization, indicating that high-pressure nebulization does not cause aggregation nor disintegration of the NPs. In contrary to size, the zeta potential was significantly altered after nebulization ( $p < 0.001$  for both 100 nm and 200 nm particles; **Figure 4C**), becoming less negatively charged.

### 2.3. Omental tissue penetration of nanoparticles after in vitro nebulization

Fluorescent nanoparticles of 100 nm and 200 nm were nebulized to compare the omental tissue penetration depth with or without EP. **Figure 5** illustrates the omental tissue penetration of 100 nm and 200 nm NPs. Tissue penetration was not affected by the electrical force in the region opposite the nebulizer (position A). However, in the tissue located opposite the nebulizer but covered by a tunnel (position B), addition of electrical force slightly increased tissue penetration of 100 and 200 nm NPs. Interestingly, the larger NPs showed a deeper tissue penetration at this position, specifically in region of interest (ROI) I (closest to the exposed surface). At the side wall of the box (position C) and, even more pronounced, at the top of the box (position D), EP significantly improved omental tissue penetration, even at a distance of up to 900  $\mu\text{m}$  from the tissue surface. In position C and D, the effect of electrical force was more pronounced when using 100 nm compared to 200 nm NPs.

### 2.4. Effects of electrostatic precipitation on mesothelial integrity and inflammation

Histological and morphometric changes of the peritoneal surface after PIPAC treatment in the rat were analysed using hematoxylin and eosin (HE) and Masson's trichrome (MT) staining as well as scanning electron microscopy (SEM) imaging, as summarized in **Figure 6A** and **Table S1**. Peritoneal samples of the untreated animal showed a typical continuous mesothelial lining with microvilli supported by a thin submesothelial layer without inflammatory changes. In all treated animals, however, thickening of the submesothelial layer was observed, caused by oedema and inflammation. Inflammation was most pronounced in the Nab-PTX treatment groups (**Figure 6B**). Minimal inflammation was observed in the parietal peritoneum of the capnoperitoneum ( $\text{CO}_2$  insufflation alone) group and saline treatment groups. In the untreated animal, SEM showed extensive and uniform microvilli on the visceral peritoneum. Insufflation of  $\text{CO}_2$  alone led to some aberrations to microvilli, including reduced density and shortening. PIPAC with Nab-PTX led to more

This article is protected by copyright. All rights reserved.



extensive mesothelial damage, as evidenced by bulging and retraction of mesothelial cells, and delamination of the mesothelium from the basement membrane. Importantly, these changes were not worsened by the application of an electrostatic field.

## 2.5. Systemic paclitaxel exposure after (e)PIPAC in the rat

Dry blood spot samples were taken after PIPAC and ePIPAC to measure systemic PTX exposure. Average systemic PTX concentrations after PIPAC and ePIPAC as a function of time are displayed in **Figure 6C**. The mean peak concentration ( $C_{max}$ ) of PTX in plasma was significantly higher ( $p = 0.050$ ) after ePIPAC compared to PIPAC and was found  $3.5 \pm 0.93$  h ( $t_{max}$ ) after initiation of the nebulization. No significant differences were observed in  $t_{max}$  between PIPAC and ePIPAC treatment. Furthermore, analysis of pharmacokinetic (PK) data showed a significantly higher ( $p = 0.007$ ) area under the curve ( $AUC_{0-24h}$ ) after ePIPAC, compared to PIPAC. A detailed overview of the PK data is represented in **Table S2**.

## 2.6. Tissue penetration depth of nanoparticle albumin-bound paclitaxel after (e)PIPAC in the rat

To visualize PTX tissue uptake, biopsies were taken four hours after PIPAC and ePIPAC. **Figure 7A** and **Figure 7C** depict the penetration depth of paclitaxel (PTX) in peritoneal tissue of rats assessed by mass spectrometry imaging (MSI) four hours after IP nebulization of Nab-PTX. The PTX signal was clearly visible at the side of the parietal peritoneum adjacent to the peritoneal cavity. EP enhanced PTX penetration in the peritoneal tissue taken at the left iliac fossa, which is not opposite to the nozzle jet of the nebulizer.

## 2.7. Tissue concentration of nanoparticle albumin-bound paclitaxel after (e)PIPAC in the rat

Peritoneal tissue samples were taken four hours after Nab-PTX administration to measure PTX tissue concentration. The distribution pattern of Nab-PTX was determined based on the PTX-concentration of tissue homogenates derived from the specimens taken at right upper abdomen (RUA), left upper abdomen (LUA), right iliac fossa (RF) and left iliac fossa (LF; **Figure 7B**). Significant differences were observed in PTX concentration ( $p = 0.003$ ) between the four abdominal quadrants after PIPAC, indicating a non-homogeneous distribution pattern. However, after EP, no significant differences in PTX concentration was observed between anatomical locations, indicating a much more homogeneous drug distribution.

## 3. Discussion

Here we report, for the first time, the potential of EP and electromotive drug transport to enhance spatial homogeneity and tissue penetration after IP aerosol delivery of nanosized medicines. There is increasing interest in IP delivery of nanomolecular drugs to treat peritoneal metastases.<sup>[5,14]</sup>

Compared to smaller drugs, nanoscale vehicles for cancer therapy afford extended circulation, reduced toxicity, controlled release, and enhanced drug protection. However, after IP delivery, transport of IP nanosized drugs into tumor tissue is hampered by the elevated interstitial fluid and solid pressures that characterize the physical tumor microenvironment.<sup>[15]</sup>

The addition of an electrical force has the potential not only to improve drug distribution throughout the peritoneal cavity during capno(CO<sub>2</sub>)peritoneum, but also to enhance tissue penetration of the drug. Electrically driven drug transport is currently used in combination with intravesical drug administration for the treatment of early stage bladder cancer (electromotive drug administration, EMDA) and in combination with transdermal drug delivery (iontophoresis).<sup>[9,16]</sup>

Using a CFD model of the kinetic behaviour of individual aerosol particles generated in a closed CO<sub>2</sub> filled cavity, we predicted that EP would significantly enhance homogeneity of drug distribution by counteracting initial velocity, drag force, and gravitational force. These predictions were validated using an in vitro model of aerosol generation combined with EP in a closed pressurized CO<sub>2</sub> environment. Since high pressure nebulization may affect the structural integrity and physicochemical properties of nanoscale drugs, we verified the effects of PIPAC on size and zeta potential of different sized NPs. While no changes in size were found, nebulization caused a modest reduction in the negative zeta potential, especially of the 100 nm NPs. This is probably explained by the triboelectric charging effect, caused by friction between the accelerated drug and the wall of the nebulizer.<sup>[17]</sup> This small change in zeta potential is unlikely to affect the pharmacokinetics of the investigated NPs. In general, a change in zeta potential does not affect stability of NPs if it does not change from negative to neutral or positive, as this could lead to early cargo release or modify binding sites.<sup>[18,19]</sup> Further research is planned in order to investigate how drug and particle charge, current and voltage intensity, and current polarity applied affect aerosol particle kinetics.

In vivo, we investigated whether IP aerosol delivery of Nab-PTX combined with EP would aggravate structural and inflammatory damage to the mesothelial lining, as observed in tissue samples obtained 24 hours after PIPAC. It is well known, indeed, that insufflation of cold and dry CO<sub>2</sub> gas into the peritoneal cavity causes multiple adverse effects on the mesothelial lining. These include oxidative stress, desiccation of the mesothelium, disruption of cell junctions and loss of glycocalyx, diminished scavenging of reactive oxygen species, decreased peritoneal blood flow, peritoneal acidosis and hypoxia, and generation of cytokines such as IL-1, IL-6, IL-8 and TNF $\alpha$ .<sup>[20]</sup> We found that insufflation of CO<sub>2</sub> caused mild damage to the mesothelial surface, as assessed by histology and electron microscopy. However, IP aerosol delivery of Nab-PTX aggravated structural damage and inflammation of the peritoneum, but these effects were not worsened by the addition of EP. Despite the observed effects of IP Nab-PTX, there is a significant clinical experience with IP paclitaxel in

patients with ovarian or gastric cancer, and a recent phase I trial using catheter based IP Nab-PTX showed limited locoregional toxicity.<sup>[21]</sup> Also, nanosized formulations of paclitaxel allow to avoid using Cremophor EL, which can cause significant hypersensitivity, in order to increase solubility.<sup>[22]</sup>

The currently used nebulizer for clinical PIPAC treatment uses a high-pressure injector, which generates approximately  $2 \times 10^6$  Pa of inlet pressure. This energy is translated into a significant initial velocity of the generated aerosol particles (16 m/s). As a consequence, it has been observed that the abdominal regions opposite the tip of the nebulizer are overexposed, while other regions remain undertreated.<sup>[23]</sup> Our data show that, in vivo, application of EP results in effective redistribution of the aerosolized Nab-PTX. At the same time, MALDI imaging of tissue Nab-PTX distribution showed that application of a high voltage DC electrical field for 30 minutes, but not one minute, resulted in significantly higher tissue penetration distance from the peritoneal surface. This is an important finding, since inadequate tissue penetration is known to be a major factor limiting the efficacy of IP drug delivery.<sup>[24]</sup> At the same time, plasma exposure was increased, which is an expected consequence of enhanced drug penetration in a perfused tissue. However, systemic PTX exposure remained well below published values after intravenous PTX administration in the rat.<sup>[25]</sup> Defining the parameters that affect electromotive drug transport after ePIPAC is a priority for future research. Similar to the recently described method of electrically enhanced local drug delivery to the pancreas, the relevant transport mechanisms likely are a combination of electrorepulsion and electroosmosis.<sup>[26,27]</sup> Obviously, the physicochemical properties of the stroma will have a major effect, and it remains to be investigated to which extent electromotive NP transport will be observed in cancer tissue.

#### 4. Conclusion

The application of an electrical field counteracts the effect of gravity on IP nebulized NPs. Therefore, the addition of EP significantly improves spatial homogeneity and drug uptake after IP aerosol delivery of nanosized drug in vitro and in vivo, without worsening the effects of CO<sub>2</sub> insufflation and IP chemotherapy on the mesothelial structural integrity. In addition, a 30-minute application of the high voltage DC electrical field significantly increases tissue penetration of aerosolized IP Nab-PTX (Abraxane®). The observed effects suggest that EP and electromotive drug transport may enhance the anticancer efficacy of PIPAC treatment in patients with PM.

## 5. Experimental Section

*In vitro model:* In vitro experiments were performed using a custom-made hermetically sealable plexiglass box with a total volume of 4 L, mimicking the patient's abdominal cavity (**Figure 8**). A GelPOINT Mini (Applied Medical, Amersfoort, The Netherlands) on the lid of the box allowed the insertion of the nebulizer and the brush electrode (Alesi Surgical, Cardiff, United Kingdom). Fresh pig omentum specimens were placed on metal plates at four different locations: on the bottom of the box (A), under a bilaterally open plastic tunnel (B), on the side wall of the box (C), and on the top of the box (D). The metal plates were connected to an electrostatic generator (Ultravision, Alesi Surgical, Cardiff, United Kingdom), which creates a voltage of 7.5–9.5 kV and current intensity of  $\leq 10 \mu\text{A}$ . The box was then tightly sealed, and a constant carbondioxide pressure of 12 mmHg was maintained using a pressure regulated insufflator. The Ultravision generator was activated at the start of aerosol injection. All nebulizations were independently conducted and the specimens were exposed to the aerosol for 30 minutes. Thereafter, the aerosol was evacuated through a closed aerosol waste system containing a 99.999% ULPA-carbon filter.

*Computational model:* Based on the dimensions of the in vitro box (185 x 135 x 152 mm<sup>3</sup>, **Figure 8**), a computational model was developed using COMSOL Multiphysics (COMSOL, Inc., Burlington, VT).

This article is protected by copyright. All rights reserved.

Tetrahedral grids were used for discretisation of the domain. Smoothing techniques were applied, and the total number of volume mesh elements was 98,798. As a first step, a stable CO<sub>2</sub> pressure of 12 mmHg was simulated. Aerosol particle motion was modelled using the Particle Tracing module of COMSOL Multiphysics with appropriate initial conditions, boundary conditions, and physical forces (gravity, drag, inertial impaction, and electromotive force). Mathematical details of the model are provided in **Figure S1 and Equation S1 to S8**.

*Measurement of spatial aerosol distribution in silico:* After a stable pneumoperitoneum of 12 mmHg was obtained in the simulation, a simulated volume of 50 mL of black ink (density 1,071.9 kg/m<sup>3</sup>, viscosity 4.875 mPa·s) was nebulized with a volumetric flow rate of 0.5 mL/s at a fixed injector position at the top of the box. Aerosol particles were injected during 40 seconds and the total simulation time was considered 30 minutes. EP (**Figure 1B**) was activated at the same time as the aerosol particle injection and it was remained until the end of the simulation. The total surface of the tissue samples was defined by the tissue geometry (20 x 20 x 2 mm<sup>3</sup>). To calculate the tissue surface coverage with black ink (%), a Measurement Accumulator was created in the Particle Tracing Module of COMSOL Multiphysics. A colour threshold was set in the Measurement Accumulator to distinguish between stained and non-stained tissue. This way, the black ink coverage could be determined at positions A, B, C and D in the CFD box model.

*Measurement of spatial aerosol distribution in vitro:* Fifty mL undiluted black ink (Pelikan nv, Groot-Bijgaarden, Belgium) was nebulized into the in vitro box at a flow rate of 0.5 mL/s and a maximal upstream injection pressure of 20 bar. Nebulizations were performed without activation of the electrostatic generator (PIPAC;  $n=6$ ), with activation of the generator for one minute (ePIPAC<sub>1 min</sub>;  $n=6$ ) or 30 minutes (ePIPAC<sub>30 min</sub>;  $n=6$ ). After the (e)PIPAC procedure, the fresh pig omentum specimens were patted dry and were placed on a white paper to take photographs (ISO200; aperture 2.65; shutter speed 1/24). The photographs were uploaded in ImageJ for pixel analysis. A

ROI was drawn around the specimen border and the number of pixels in the ROI was calculated.

Thereafter, the colour brightness threshold was set on 1 – 100 to select the black coloured pixels.

The proportion (%) of stained specimen was calculated by **Equation 1**:

$$\text{proportion stained (\%)} = \frac{\text{number of black stained pixels in ROI}}{\text{total number of pixels in ROI}} \times 100\% \quad (1)$$

After obtaining digital images, omental specimens were embedded in optimal cutting temperature (OCT) compound embedding medium, and cryosections of 20 µm were made using a microtome-cryostat (Leica CM 1100, Leica Biosystems, Mount Waverly, Australia). Using a light microscope, each cryosection was scored by three blinded and independent observers for the amount of ink visible on the tissue surface using a light microscope. The following scoring system was used: 0 = no ink visible; 0.5 = hardly visible or interrupted line; 1 = clear visible line.

*Measurement of size distribution of nanoparticles:* Fluorescently labelled nanoparticles (Molecular Probes® Carboxylated FluoSpheres®; Thermo Fisher Scientific, Carlsbad, United States) with a hydrodynamic diameter of 100 nm and 200 nm were sonicated (2510 Branson Sonicator, Marshall Scientific, Hampton, New Hampshire, United States) for 25 minutes and were subsequently diluted in distilled water. The NPs were nebulized (Capnopen®, Capnomed, Zimmern, Germany) and collected after the nebulization procedure. Size distribution of nebulized ( $n=3$ ) and non-nebulized ( $n=3$ ) samples was measured using the Nanosight LM 10 (Malvern Panalytical, Herrenberg, Germany) and Malvern Zetasizer nano-ZS (Malvern Instruments, Worcestershire, United Kingdom). Size measurements were performed with five runs per replicate and presented as the median hydrodynamic diameter ( $D50$ ). Zeta potential measurements were done with three runs per replicate.

*Measurement of in vitro penetration depth:* Fluorescently labelled nanoparticles with a hydrodynamic diameter of 100 nm and 200 nm were nebulized in the in vitro box with a flow rate of

0.5 mL/s and a maximal upstream injection pressure of 20 bar without electrostatic aerosol precipitation (PIPAC;  $n=6$ ) or with electrostatic aerosol precipitation for 30 minutes (ePIPAC;  $n=6$ ). Omental specimens were embedded in OCT compound embedding medium (Leica microsystems, Machelen, Belgium) and cryosectioned at a thickness of 20  $\mu\text{m}$ . Cryosections were equilibrated at room temperature, washed with Dulbecco's phosphate-buffered saline (DPBS-, Fisher Scientific, Merelbeke, Belgium) and edited with Vectashield mounting medium (Vector Laboratories, Inc. Burlingame, California, United States). Cryosections were imaged with fluorescence confocal microscopy (Nikon C2, Nikon Instruments Inc., Amstelveen, The Netherlands), and images were processed and analysed with ImageJ (version 1.51, National Institutes of Health, Bethesda, Maryland, United States). Congruent ROIs ( $500 \times 300 \mu\text{m}^2$ ) were drawn below each other to measure the mean fluorescence intensity (MFI) on different tissue depths: 0 – 300  $\mu\text{m}$  (ROI I), 300 – 600  $\mu\text{m}$  (ROI II) and 600 – 900  $\mu\text{m}$  (ROI III). Series of ROI I, II and III were drawn in triplicate on each cryosection with an intermediate distance of 500  $\mu\text{m}$ .

*In vivo model of intraperitoneal aerosol delivery of nanoparticle paclitaxel:* All animal experiments were approved by the Animal Ethics Committee of the Faculty of Medicine at Ghent University (ECD 18-30) and were performed according to relevant Belgian and European animal welfare regulations. Male adult Wistar Hannover rats ( $n=36$ ; Envigo, Horst, The Netherlands) were allowed to acclimatize to the surroundings for at least seven days and were kept in standard housing conditions with water and food at libitum and a 12 h light/dark cycle. Rats were evaluated daily for pain or discomfort based on the rat grimace scale and body weight. All procedures were performed under general inhalation anaesthesia (Sevorane<sup>®</sup>, Abbott, Belgium; 8 vol% induction, 4 vol% maintenance), and analgesia (ketoprofen, 5 mg/kg, subcutaneously) was administered if necessary. After the experiments, all rats were sacrificed with a lethal injection of T-61 (0.3 mL/kg, intravenously) into the tail vein.



Animals were randomly divided into six groups: PIPAC with Nab-PTX (Abraxane<sup>®</sup>, Celgene Europe, Uxbridge, United Kingdom; 24 mg/kg;  $n=16$ ), ePIPAC with Nab-PTX (24 mg/kg;  $n=16$ ), PIPAC with saline ( $n=1$ ), ePIPAC with saline ( $n=1$ ), insufflation of carbondioxide without drug nebulization (capnoperitoneum;  $n=1$ ) and no treatment ( $n=1$ ). The (e)PIPAC procedures were performed as previously described.<sup>[28]</sup> Briefly, 5 mm and 11 mm balloon trocars (Kii, advanced fixation sleeve, Applied Medical, Amersfoort, The Netherlands) were inserted into the abdomen and a constant capnoperitoneum pressure of 8 mmHg was established (Olympus UHI-3 insufflator, Olympus Surgical Technologies Europe, Hamburg, Germany; **Supplementary Figure S2**). A laparoscope and nebulizer were introduced to the 5 mm and 11 mm trocar, respectively. Injection parameters were set at a flow rate of 0.8 mL/s and a maximal upstream injection pressure of 20 bar. The capnoperitoneum pressure of 8 mmHg was maintained for 30 minutes. In the ePIPAC treatment groups, the Ultravision™ generator was activated at the start of aerosol generation and the electric current was maintained for 30 minutes. Thereafter, the aerosol was evacuated through a closed aerosol waste system containing a 99.999% ULPA-carbon filter. Finally, trocars were removed, and the laparoscopic procedure was terminated. The incisions were closed with a two-layered running suture (Vicryl Plus 4-0 Ethicon, Johnson & Johnson international, Sint-Stevens-Woluwe, Belgium) and analgesia was administered. Eight rats of the PIPAC Nab-PTX treatment group and eight rats of the ePIPAC Nab-PTX treatment group were sacrificed four hours after Nab-PTX administration, while all the other rats were sacrificed 24 hours after (e)PIPAC.

*Histopathological analysis of the peritoneum:* Samples for histopathological examination were taken from the parietal peritoneum at RUA, LUA, RF and LF 24 hours after every (e)PIPAC procedure. All samples were immediately fixed by immersion in 4% paraformaldehyde in PBS for 72 hours and embedded in paraffin. Tissues were then serially sectioned for standard HE and MT staining. Morphological changes of the parietal peritoneum were observed by light microscopy. Inflammation

was scored by a trained pathologist as follows: 0 = no inflammation; 1 = minimal inflammation; 2 = moderate inflammation; and 3 = strong inflammation.

*Scanning electron microscopy of the peritoneum:* Samples of parietal peritoneum at the central region of the abdomen and visceral peritoneum at the upper ileum were obtained 24 hours after the (e)PIPAC procedure. Biopsies were immersed in a (4-(2-hydroxyethyl)-1-piperazineethanesulfonic acid (HEPES) buffered mixture of glutaraldehyde and paraformaldehyde (Fisher Scientific, Merelbeke, Belgium) for 24 hours. Fixed tissues were rinsed with distilled water, post-fixed for two hours in 1% osmium tetroxide, and washed again with distilled water. Next, samples were dehydrated in increasing ethanol series followed by increasing ethanol-acetone series up to pure acetone (VWR international, Oud-Heverlee, Belgium). Specimens were then subjected to critical point drying (Balzers CPD 030, Sercolab, Merksem, Belgium) using liquid carbondioxide substitution. Samples were mounted on aluminium plates and sputter-coated (JEOL JFC 1300 Auto Fine Coater, Jeol, Zaventem, Belgium) with platinum. The samples were examined using a scanning electron microscope (JEOL JSM 5600 LV, Jeol, Zaventem, Belgium).

*Measurement of paclitaxel penetration depth in in vivo peritoneal tissue:* Biopsies of parietal peritoneum were taken at the RUA, LUA, RF and LF four hours after (e)PIPAC, snap-frozen in liquid nitrogen and stored at -80 °C until imaging was performed. The spatial distribution of PTX in the parietal peritoneum was determined by MSI according to the method developed by Giordano and colleagues.<sup>[29]</sup> Frozen samples were cut into 10 µm sections using a cryo-microtome and mounted on pre-cooled matrix-assisted laser desorption/ionization (MALDI) plates (Opti-TOF 384 Well insert). Subsequently, plates were dried during one hour in a vacuum drier at room temperature and then sprayed with a titanium dioxide matrix suspension (Evonik, Essen, Germany) containing deuterated PTX (D5-PTX, Toronto Research, Toronto, Canada) as internal standard. MSI analysis was performed using a MALDI 4800 TOF-TOF (AB SCIEX Old Connecticut Path, Framingham, MA, United States). The

penetration depth of PTX was calculated from the side of a square ROI, with an area drawn and calculated using Tissue View software 1.1 (AB SCIEX Old Connecticut Path, Framingham, MA, United States).

*Measurement of paclitaxel concentration in in vivo tissue samples:* Samples were taken from the parietal peritoneum at the RUA, LUA, RF and LF four hours after (e)PIPAC, washed in saline solution, snap-frozen in liquid nitrogen and stored at -80 °C until high-performance liquid chromatography (HPLC) analysis. Quantitative analysis of PTX was assessed by HPLC as previously described.<sup>[29]</sup> Briefly, tissues were homogenized in 0.2 M ammonium acetate pH 4.5 (1:3 wt/vol) and 0.5 mL of homogenate for each sample was assayed together with a five points of standard calibration curve prepared in untreated control tissues at concentrations ranging from 0.25 to 2.5 µg/sample. The limit of quantification (LOQ) was 0.05 µg/sample.

*Measurement of systemic paclitaxel exposure in vivo:* Blood microsamples were collected from the tail vein at the start of nebulization and 15, 30, and 60 minutes and 1.5, 2, 4, 6, and 24 hours after each (e)PIPAC procedure. Ten µL of blood was spotted on a blood spot card (Perkin Elmer 226 Bioanalysis RUO Card, Perkin Elmer, Greenville, United States). Dried blood spots (DBS) were punched out and collected in Eppendorf tubes. After adding 200 µL of internal standard solution mix (2 ng/mL), the samples were continuously shaken at 500 RPM for 20 minutes at 37 °C by a thermoshaker. Thereafter, 100 µL of the resulting solution was diluted with 100 µL of water (ULC-MS water, Biosolve, Valkenswaard, The Netherlands). The PTX concentration of DBS samples was determined by a previously developed ultra-performance liquid chromatography -tandem mass spectrometry method (UPLC-MS/MS).<sup>[30]</sup> The lower limit of quantification of PTX in a DBS samples was 1 ng/mL.

*Statistical analysis:* Data are presented as mean (standard deviation). Sample sizes were n=6 for in vitro box model experiments, n=3 in charge and size distribution experiments and n=8 in in vivo

experiments. Data distribution was tested for normality with the Shapiro-Wilk test. Comparisons of means of two groups were performed with the Student t-test or Mann-Whitney U test, while comparisons between three or more groups were performed with one-way repeated measurement ANOVA. P-values were calculated with Graphpad Prism™ 7 (Graphpad software, La Jolla, United States) and a p-value of  $\leq 0.05$  was considered to indicate statistical significance.

### **Supporting Information**

Supporting Information is available from the Wiley Online Library or from the author.

## Acknowledgements

The authors declare no conflict of interest. The authors acknowledge the lab technicians Sabine De Groote and Silke Willekens for conduction of HE staining and the lab of pathology for conduction of MT staining. We also thank the department of morphology of the faculty of veterinary medicine (Bart De Pauw) and the centre for microsystems technology (CMST; Dieter Cuypers) of Ghent University for providing their scanning electron microscope. Margot Ceelen is thanked for providing Figure S2. Helena Braet is a doctoral fellow from the Fund for Scientific Research Flanders (FWO-SB). Wim Ceelen is a senior clinical researcher from the Fund for Scientific Research - Flanders (FWO). Wim Ceelen and Katrien Remaut are supported by a Concerted Research Action of Ghent University (G061119N). Charlotte Debbaut is supported by a postdoctoral fellowship from the Scientific Research Flanders (1202418N), and a starting grant from the special research fund of Ghent University (BOF/STA/201909/015).

Received: ((will be filled in by the editorial staff))

Revised: ((will be filled in by the editorial staff))

Published online: ((will be filled in by the editorial staff))

## References

- [1] M. Alyami, M. Hübner, F. Grass, N. Bakrin, L. Villeneuve, N. Laplace, G. Passot, O. Glehen, V. Kepelekian, *The Lancet Oncology* **2019**, *20*, e368.
- [2] G. Nadiradze, P. Horvath, Y. Sautkin, R. Archid, F.-J. Weinreich, A. Königsrainer, M. A. Reymond, *Cancers* **2019**, *12*, 34.
- [3] M. Shariati, W. Willaert, W. Ceelen, S. C. De Smedt, K. Remaut, *Cancers (Basel)* **2019**, *11*, DOI 10.3390/cancers11070906.
- [4] G. R. Dakwar, M. Shariati, W. Willaert, W. Ceelen, S. C. De Smedt, K. Remaut, *Advanced Drug Delivery Reviews* **2017**, *108*, 13.
- [5] L. Van de Sande, S. Cosyns, W. Willaert, W. Ceelen, *Drug Deliv* **2019**, *27*, 40.
- [6] A. Bellendorf, V. Khosrawipour, T. Khosrawipour, S. Siebigteroth, J. Cohnen, D. Diaz-Carballo, A. Bockisch, J. Zieren, U. Giger-Pabst, *Surg Endosc* **2017**, *1*.
- [7] W. Willaert, L. Van de Sande, E. Van Daele, D. Van De Putte, Y. Van Nieuwenhove, P. Pattyn, W. Ceelen, *European Journal of Surgical Oncology* **2019**, *45*, 2302.
- [8] T. Kakchekeeva, C. Demtröder, N. I. Herath, D. Griffiths, J. Torkington, W. Solaß, M. Dutreix, M. A. Reymond, *Ann Surg Oncol* **2016**, *23*, 592.
- [9] J. H. Jung, A. Gudeloglu, H. Kiziloğlu, G. M. Kuntz, A. Miller, B. R. Konety, P. Dahm, *Cochrane Database Syst Rev* **2017**, *2017*, DOI 10.1002/14651858.CD011864.pub2.
- [10] B. Kos, J. L. Vásquez, D. Miklavčič, G. G. G. Hermann, J. Gehl, *PeerJ* **2016**, *4*, e2309.
- [11] K. Ita, *Pharmaceutics* **2016**, *8*, DOI 10.3390/pharmaceutics8010009.
- [12] P. G. Koullapis, S. C. Kassinos, M. P. Bivolarova, A. K. Melikov, *Journal of Biomechanics* **2016**, *49*, 2201.
- [13] M. J. Telko, J. Kujanpää, A. J. Hickey, *International Journal of Pharmaceutics* **2007**, *336*, 352.
- [14] W. Ceelen, H. Braet, G. van Ramshorst, W. Willaert, K. Remaut, *Expert Opinion on Drug Delivery* **2020**, *0*, 1.
- [15] L. C. Böckelmann, U. Schumacher, *Expert Opinion on Therapeutic Targets* **2019**, *23*, 1005.
- [16] N. Akhtar, V. Singh, M. Yusuf, R. A. Khan, *Biomedical Engineering / Biomedizinische Technik* **2020**, *0*, DOI 10.1515/bmt-2019-0019.
- [17] S. Matsusaka, H. Maruyama, T. Matsuyama, M. Ghadiri, *Chemical Engineering Science* **2010**, *65*, 5781.

- [18] A.-K. Minnaert, G. R. Dakwar, J. M. Benito, J. M. García Fernández, W. Ceelen, S. C. De Smedt, K. Remaut, *Macromol. Biosci.* **2017**, *17*, 1700024.
- [19] M. Shariati, H. Zhang, L. Van de Sande, B. Descamps, C. Vanhove, W. Willaert, W. Ceelen, S. C. De Smedt, K. Remaut, *Pharm Res* **2019**, *36*, 126.
- [20] S. Carpinteri, S. Sampurno, M.-P. Bernardi, M. Germann, J. Malaterre, A. Heriot, B. A. Chambers, S. E. Mutsaers, A. C. Lynch, R. G. Ramsay, *Ann Surg Oncol* **2015**, *22*, 1540.
- [21] M. C. Cristea, P. Frankel, T. Synold, S. Rivkin, D. Lim, V. Chung, J. Chao, M. Wakabayashi, B. Paz, E. Han, et al., *Cancer Chemother Pharmacol* **2019**, *83*, 589.
- [22] A. M. Khalifa, M. A. Elsheikh, A. M. Khalifa, Y. S. R. Elnaggar, *Journal of Controlled Release* **2019**, *311–312*, 125.
- [23] V. Khosrawipour, T. Khosrawipour, D. Diaz-Carballo, E. Förster, J. Zieren, U. Giger-Pabst, *Annals of Surgical Oncology* **2016**, *23*, 1220.
- [24] N. Lagast, C. Carlier, W. P. Ceelen, *Surgical Oncology Clinics of North America* **2018**, *27*, 477.
- [25] S. Bhattacharya, P. Sarkar, J. Khanam, T. K. Pal, *Journal of Chromatography B* **2019**, *1124*, 331.
- [26] R. H. Guy, Y. N. Kalia, M. B. Delgado-Charro, V. Merino, A. López, D. Marro, *Journal of Controlled Release* **2000**, *64*, 129.
- [27] J. D. Byrne, J. J. Yeh, J. M. DeSimone, *Journal of Controlled Release* **2018**, *284*, 144.
- [28] L. Van de Sande, W. Willaert, S. Cosyns, K. De Clercq, M. Shariati, K. Remaut, W. Ceelen, *BMC Cancer* **2019**, *19*, 424.
- [29] S. Giordano, L. Morosi, P. Veglianese, S. A. Licandro, R. Frapolli, M. Zucchetti, G. Cappelletti, L. Falcicola, V. Pifferi, S. Visentin, et al., *Scientific Reports* **2016**, *6*, 37027.
- [30] F. Xie, E. De Thaye, A. Vermeulen, J. Van Bocxlaer, P. Colin, *Journal of Pharmaceutical and Biomedical Analysis* **2018**, *148*, 307.

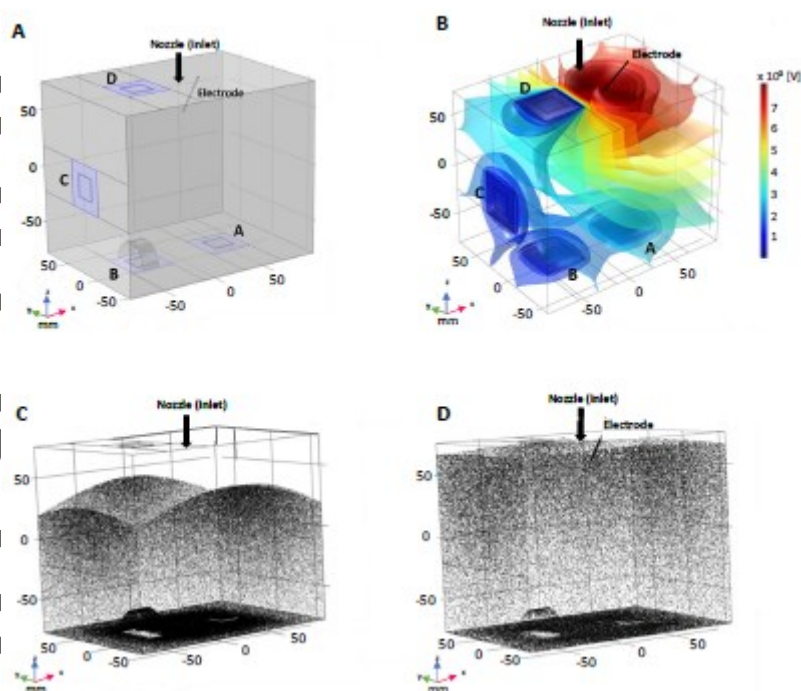


**Figure 1.** In silico aerosol distribution pattern. A: Box model with simulated metal tissue fixing plates at the bottom of the box (A), under a bilaterally open plastic tunnel (B), at the side wall of the box (C), and at the top of the box (D). B: Visualization of the electrical field in the box. Computational fluid dynamics simulation of the aerosol droplet distribution in the box model is demonstrated without electrostatic precipitation (PIPAC; panel C) and with electrostatic precipitation (ePIPAC, panel D).



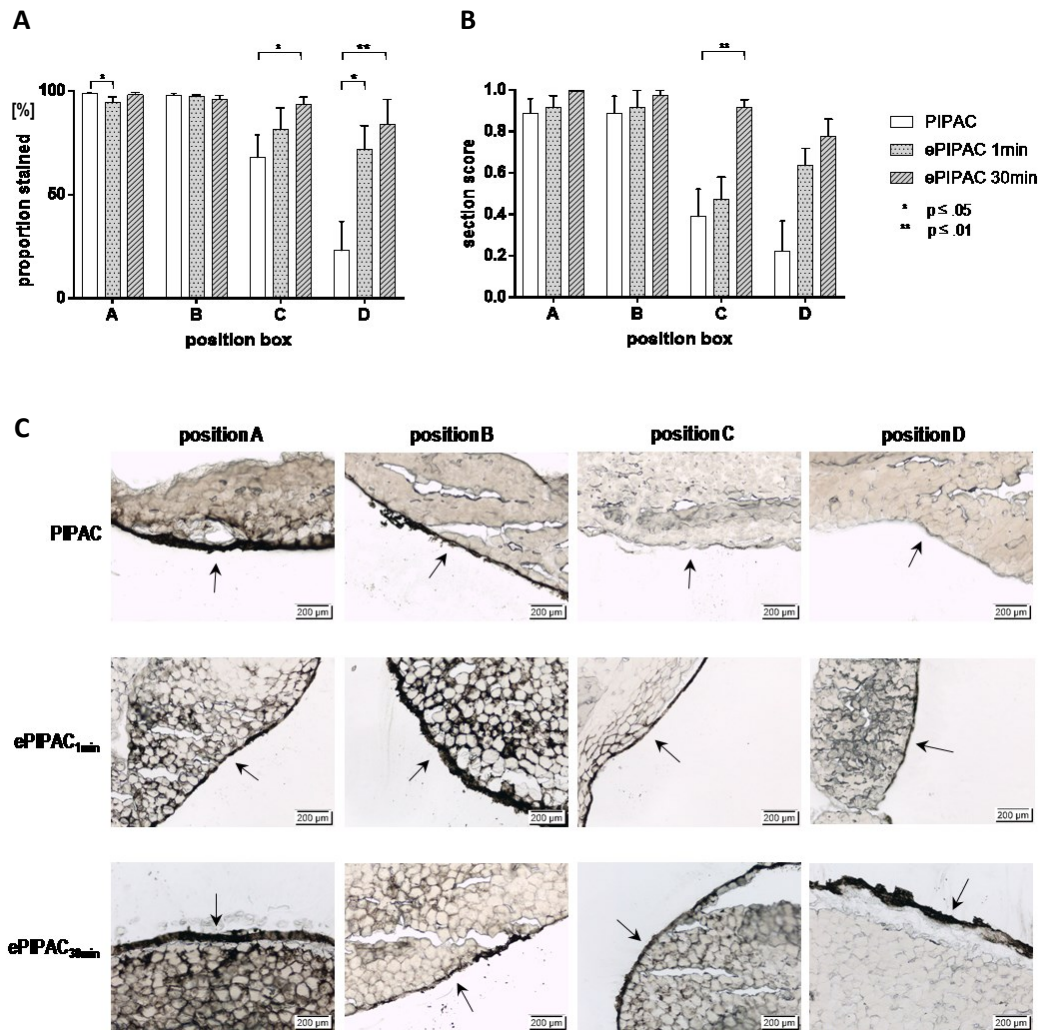


**Figure 2.** In vitro aerosol distribution pattern. A Bars indicate the proportion stained of specimens after PIPAC (n=6; white bars), ePIPAC with one-minute generator activation (n=6; dotted light grey bars) or 30 minutes activation (n=6; shaded dark grey bars). B Bars indicate the section score of cryosections after PIPAC (n=6) or ePIPAC (n=6): 0 = no ink visible; 0.5 = hardly visible or interrupted line; 1 = clear visible line. Error bars show one-time standard deviation. C Microscopic overview of cryosections after PIPAC and ePIPAC. Black arrows indicate the exposed tissue surface. The scale bar is as indicated.

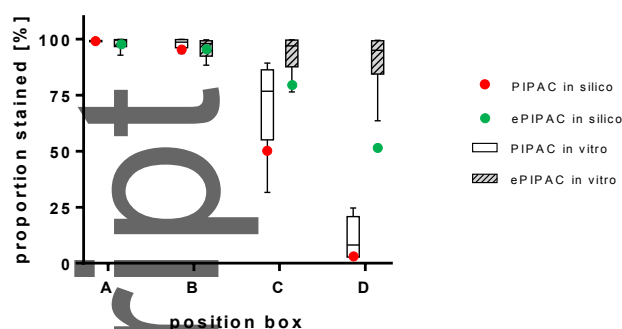


**Figure 3.** Comparison of in silico and in vitro results. The dots represent the in silico black ink coverage, while box plots show black ink coverage after in vitro nebulization. The results of black ink coverage calculated by the measurement accumulator in COMSOL Multiphysics agree with the findings calculated by ImageJ after in vitro nebulization.

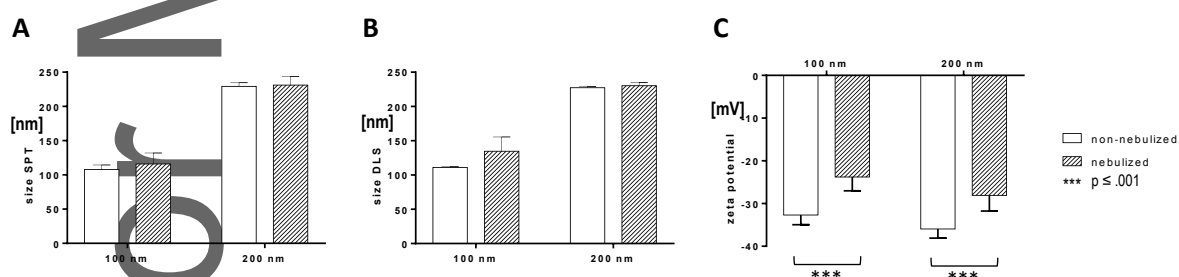


**Figure 4.** Stability of nanoparticles. Characteristics of nanoparticles before (non-nebulized;  $n=3$ ; white bars) and after (nebulized;  $n=3$ ; shaded bars) high-pressure nebulization. Mean D50 of 100 nm and 200 nm nanoparticles is presented after single particle tracking (SPT) (A) and dynamic light scattering (DLS) analysis (B). Zeta potential of 100 nm and 200 nm nanoparticles (C). Non-significant differences ( $p \geq 0.05$ ) were not indicated. Error bars represent one-time standard deviation.

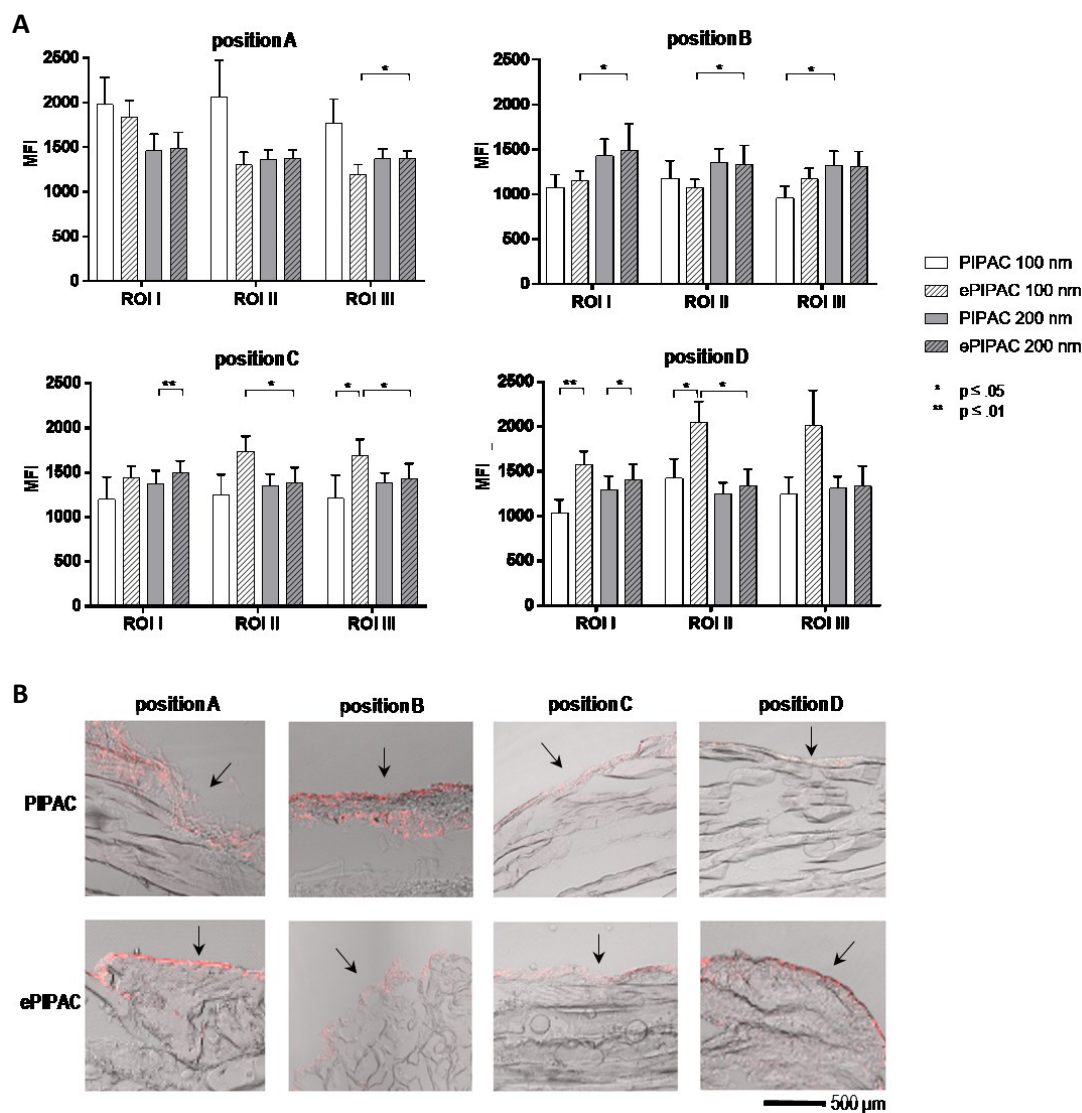


**Figure 5.** Omental tissue penetration of 100 nm and 200 nm nanoparticles. A Mean fluorescence intensity (MFI) on different tissue depths: 0 – 300  $\mu\text{m}$  (ROI I), 300 – 600  $\mu\text{m}$  (ROI II) and 600 – 900  $\mu\text{m}$  (ROI III) after PIPAC (n=6; non-shaded bars) and ePIPAC (n=6; shaded bars) for 100 nm particles (white bars) and 200 nm particles (grey bars). Non-significant differences ( $p \geq 0.05$ ) were not indicated. Error bars represent the standard deviation. B Fluorescence microscopy images of 100 nm nanoparticle (red dots) uptake after PIPAC and ePIPAC. Black arrows indicate the exposed tissue surface. The scale bar is as indicated.

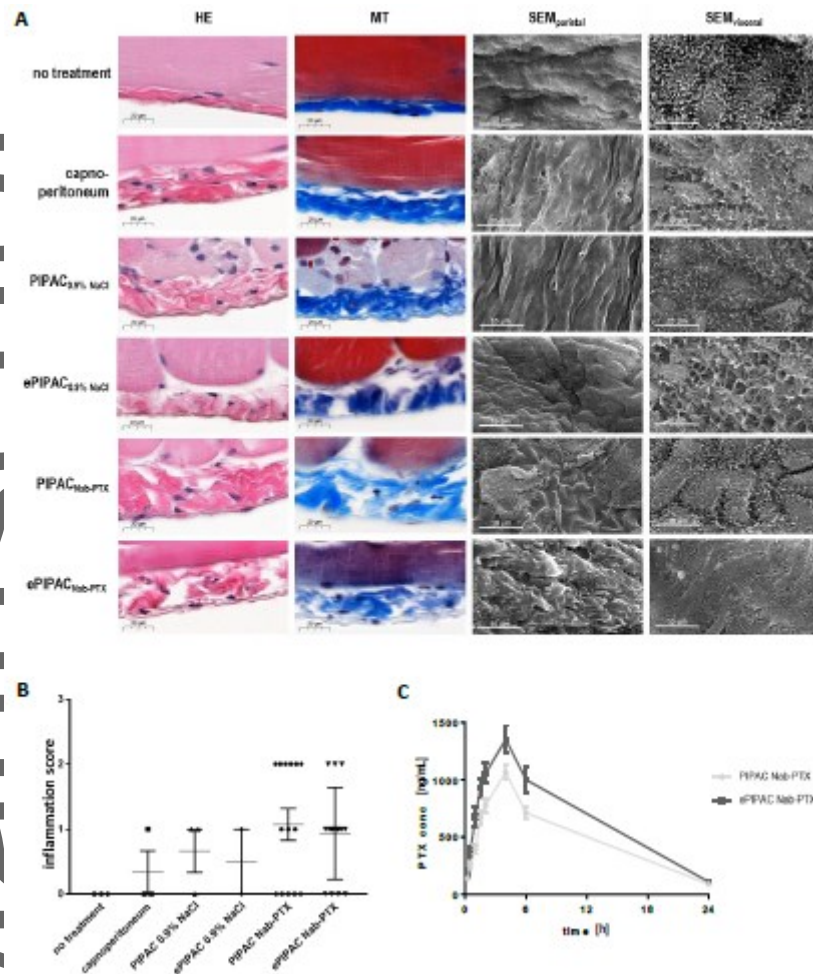


**Figure 6.** A: Structural changes of the peritoneum after (e)PIPAC in a rat model. Hematoxylin and eosin staining, HE; Masson's trichrome staining, MT; scanning electron microscopy imaging, SEM) and visceral peritoneum (SEM). The scale bars are as indicated. B: Inflammatory changes of the peritoneal surface after (e)PIPAC in the rat. Inflammation was scored as follows: 0 = no inflammation; 1 = minimal inflammation; 2 = moderate inflammation; 3 = strong inflammation. All differences were non-significant ( $p > 0.05$ ). C: Plasma exposure of PTX. Concentration (ng/mL) paclitaxel (PTX) in plasma as a function of time after PIPAC ( $n=8$ ) or ePIPAC ( $n=8$ ). Error bars represent the standard deviation.

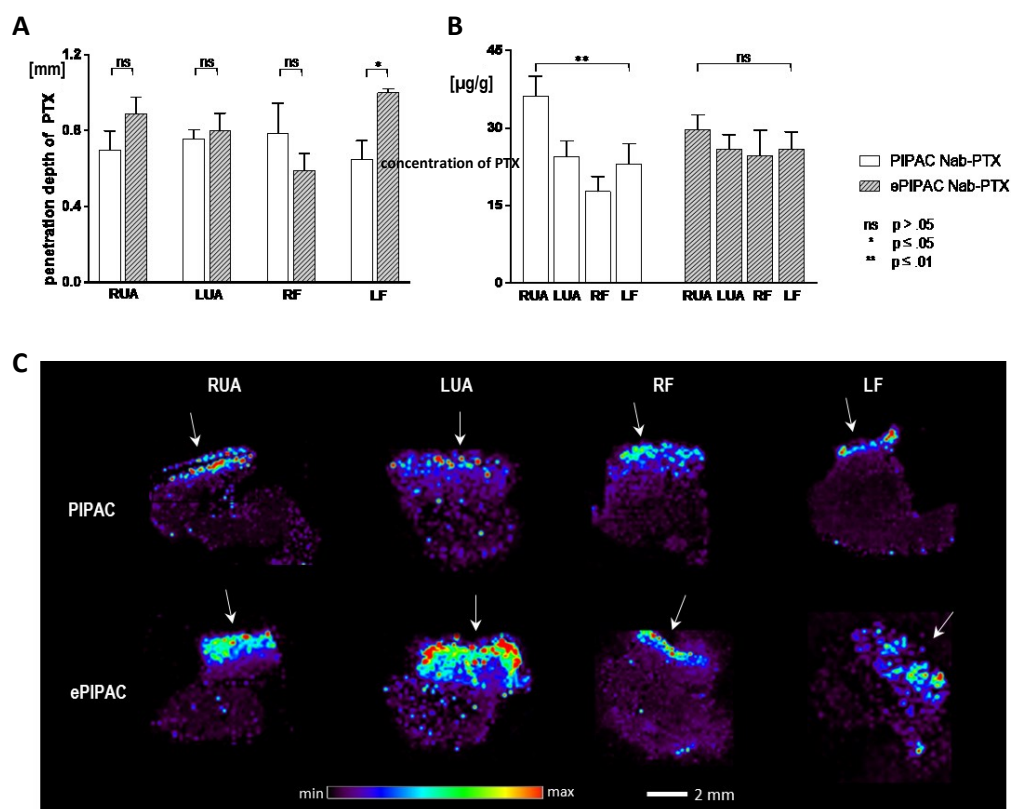


**Figure 7.** In vivo distribution of paclitaxel. A Bars indicate penetration depth of paclitaxel (PTX) four hours after PIPAC (n=8; white bars) or ePIPAC (n=8; grey bars) procedure. B Quantitative analysis of PTX four hours after PIPAC (n=8; white bars) or ePIPAC (n=8; grey bars) procedure. Error bars show one-time standard deviation. C MALDI/MS images of tissue samples taken at each quadrant four hours after PIPAC or ePIPAC procedure. Scale bar is as indicated. White arrows indicate exposed tissue surface. Samples were taken at right upper abdomen (RUA), left upper abdomen (LUA), right iliac fossa (RF) or left iliac fossa (LF).

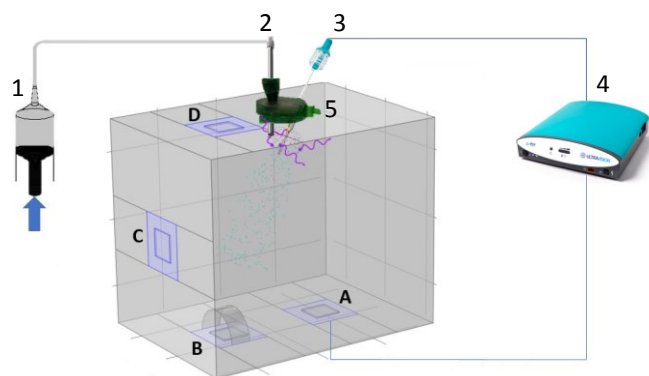


**Figure 8.** Schematic representation of the in vitro model. A plexiglass box is equipped with a laparoscopic access device, allowing the introduction of a nebulizer, connected to a high-pressure injector, and the negatively charged brush electrode. Metal tissue holding plates (A-D) are fixed to the bottom, side wall, and top of the box and connected with the electrical generator. 1. High pressure injector; 2. Nebulizer; 3. Brush electrode; 4. Electrostatic generator; 5. Access port.



In theory, the combination of electrostatic precipitation with PIPAC, termed ePIPAC, could result in better tissue penetration of the aerosol. This theoretical advantage is confirmed in this project using a CFD model, an in vitro box model and an in vivo rat model. Moreover, the peritoneal integrity was not affected by the applied electrostatic forces.

**Keyword** intraperitoneal drug delivery

Leen Van de Sande, Mohammad Rahimi-Gorji, Silvia Giordano, Enrico Davoli, Cristina Matteo, Sönke Detlefsen, Katharina D'Herde, Helena Braet, Molood Shariati, Katrien Remaut, Feifan Xie, Charlotte Debbaut, Ghader Ghorbaniasl, Sarah Cosyns, Wouter Willaert, Wim Ceelen\*

**Title** Electrostatic Intraperitoneal Aerosol Delivery of Nanoparticles: Proof of Concept and Preclinical validation

